

Fig. 5. State variations of each robot in Simulation 3.

tive errors rising from wheels slippage and imperfect communication, in this paper, the robots do not have a global coordinate system and no information is allowed to exchange. A distributed approach called LILCS is proposed. The approach is independent of the environment, and can cope with unexpected events. Each robot makes its own decisions by analyzing its ambient situation. The cooperation may emerge by local interactions among the robots. Simulations show the effectiveness of the LILCS approach.

REFERENCES

- [1] Y. U. Cao, A. S. Fukunaga, and A. B. Kahng, "Cooperative mobile robotics: Antecedents and directions," *Auton. Robots*, vol. 4, no. 1, pp. 7–27, 1997.
- [2] M. J. Mataric, "Coordination and learning in multirobot systems," *IEEE Intell. Syst. Mag.*, vol. 13, no. 2, pp. 6–8, 1998.
- [3] H. Yamaguchi, "A cooperative hunting behavior by mobile-robot troops," *Int. J. Robot. Res.*, vol. 18, no. 8, pp. 931–940, 1999.
- [4] H. Yamaguchi and T. Arai, "Distributed and autonomous control method for generating shape of multiple mobile robot group," in *Proc. IEEE/RSJ Int. Conf. Intell. Robots Syst.*, Munich, Germany, 1994, pp. 800–807.
- [5] P. Pirjanian and M. J. Mataric, "Multi-robot target acquisition using multiple objective behavior coordination," in *Proc. IEEE Int. Conf. Robot. Autom.*, San Francisco, CA, 2000, pp. 2696–2702.
- [6] E. Osawa, "A metalevel coordination strategy for reactive cooperative planning," in *Proc. 1st Int. Conf. Multi-Agent Syst.*, 1995, pp. 297–303.
- [7] J. Denzinger and M. Fuchs, "Experiments in learning prototypical situations for variants of the pursuit game," in *Proc. Int. Conf. Multi-Agent Syst.*, 1996, pp. 48–55.
- [8] M. Tan, "Multi-agent reinforcement learning: independent vs. cooperative agents," in *Proc. 10th Int. Conf. Mach. Learning*, 1993, pp. 330–337.
- [9] N. Ono, K. Fukumoto, and O. Ikeda, "Collective behavior by modular reinforcement-learning animats," in *Proc. 4th Int. Conf. Simul. Adapt. Behav.*, 1996, pp. 618–624.
- [10] J. Hespanha, H. Kim, and S. Sastry, "Multiple-agent probabilistic pursuit-evasion games," in *Proc. 38th IEEE CDC*, 1999, pp. 2432–2437.
- [11] S. Rashid, "Design and Implementation of Multi-Agent Control: Pursuit and Map Building," Master's thesis, Univ. California, Berkeley, CA, 2000.
- [12] S. Rashid and J. Kim, "Multiple-Agent Probabilistic Pursuit-Evasion Games in 2.5D Univ. California, Berkeley, CA, Tech. Rep. UCB/ERL M99/34, 1999.
- [13] R. Vidal, S. Rashid, C. Sharp, O. Shakernia, J. Kim, and S. Sastry, "Pursuit-evasion games with unmanned ground and aerial vehicles," in *Proc. IEEE Int. Conf. Robot. Autom.*, 2001, pp. 2948–2955.
- [14] R. Vidal, O. Shakernia, H. J. Kim, D. H. Shim, and S. Sastry, "Probabilistic pursuit-evasion games: theory, implementation, and experimental evaluation," *IEEE Trans. Robot. Autom.*, vol. 18, no. 5, pp. 662–669, Oct. 2002.

Homography-Based Visual Servo Tracking Control of a Wheeled Mobile Robot

Jian Chen, Warren E. Dixon, Darren M. Dawson, and Michael McIntyre

Abstract—A visual servo tracking controller is developed in this paper for a monocular camera system mounted on an underactuated wheeled mobile robot (WMR) subject to nonholonomic motion constraints (i.e., the camera-in-hand problem). A prerecorded image sequence (e.g., a video) of three target points is used to define a desired trajectory for the WMR. By comparing the target points from a stationary reference image with the corresponding target points in the live image and the prerecorded sequence of images, projective geometric relationships are exploited to construct Euclidean homographies. The information obtained by decomposing the Euclidean homography is used to develop a kinematic controller. A Lyapunov-based analysis is used to develop an adaptive update law to actively compensate for the lack of depth information required for the translation error system. Experimental results are provided to demonstrate the control design.

Index Terms—Lyapunov methods, mobile robot, nonholonomic, visual servo control.

I. INTRODUCTION

Wheeled mobile robots (WMRs) are often required to execute tasks in environments that are unstructured. Due to the uncertainty in the environment, numerous researchers have investigated different sensing methodologies as a means to enable improved autonomous response by the system. Given this motivation, researchers initially targeted the use of a variety of sonar- and laser-based sensors. Some initial work also targeted the use of a fusion of various sensors to build a map of the environment for WMR navigation (see [19], [22], [34], [36], [38], and the references within; other early innovative mobile robot control research is given in [20]). While this is still an active area of research, various shortcomings associated with these technologies and recent advances in image extraction/interpretation technology and advances in control theory have motivated researchers to investigate the sole use of camera-based vision systems for autonomous navigation. For example, using consecutive image frames and an object database, the authors of [21] recently proposed a monocular visual servo tracking controller for WMRs based on a linearized system of equations and extended Kalman filtering (EKF) techniques. Also, using EKF techniques on the linearized kinematic model, the authors of [8] used feedback from a monocular omnidirectional camera system (similar to [1]) to enable

Manuscript received February 9, 2004; revised June 14, 2004. This paper was recommended for publication by Associate Editor F. Chaumette and Editor S. Hutchinson upon evaluation of the reviewers' comments. This work was supported in part by the National Science Foundation under Grant DMI-9457967, in part by the Office of Naval Research under Grant N00014-99-1-0589, in part by a DOC Grant, in part by an ARO Automotive Center Grant at Clemson University, and in part by the Air Force Office of Scientific Research under Contract F49620-03-1-0381 at the University of Florida. This paper was presented in part at the IEEE/RSJ International Conference on Intelligent Robots and Systems, Las Vegas, NV, October 2003.

J. Chen is with the Department of Mechanical and Aeronautical Engineering, Clarkson University, Potsdam, NY 13699-5725 USA (e-mail: jian.chen@iecc.org).

W. E. Dixon is with the Department of Mechanical and Aerospace Engineering, University of Florida, Gainesville, FL 32611 USA.

D. M. Dawson and M. McIntyre are with the Department of Electrical and Computer Engineering, Clemson University, Clemson, SC 29634 USA.

Digital Object Identifier 10.1109/TRO.2006.862476

wall following, follow-the-leader, and position regulation tasks. In [18], Hager *et al.* used a monocular vision system mounted on a pan-tilt-unit to generate image-Jacobian and geometry-based controllers by using different snapshots of the target and an epipolar constraint. As stated in [2], a drawback of the method developed in [18] is that the system equations became numerically ill-conditioned for large pan angles. Given this shortcoming, Burschka and Hager [2] used a spherical image projection of a monocular vision system that relied on teaching and replay phases to facilitate the estimation of the unknown object height parameter in the image-Jacobian by solving a least-squares problem. Spatio-temporal apparent velocities obtained from an optical flow of successive images of an object were used in [33] to estimate the depth and time-to-contact to develop a monocular vision “guide robot” that is used as a guide for blind users. A similar optical flow technique was also used in [24]. In [11], Dixon *et al.* used feedback from an uncalibrated, fixed (ceiling-mounted) camera to develop an adaptive tracking controller for a WMR that compensated for the parametric uncertainty in the camera and the WMR dynamics. An image-based visual servo controller that exploits an object model was proposed in [37] to solve the WMR tracking controller (the regulation problem was not solved due to restrictions on the reference trajectory) that adapted for the constant, unknown height of an object moving in a plane through Lyapunov-based techniques. In [35], an image-based visual servo controller was proposed for a mobile manipulator application; however, the result requires geometric distances associated with the object to be known and relies on an image-Jacobian that contains singularities for some configurations. Moreover, the result in [35] requires the additional degrees of freedom from the manipulator to regulate the orientation of the camera. In [25] and [41], visual servo controllers were recently developed for systems with similar underactuated kinematics as WMRs. Specifically, Mahony and Hamel [25] developed a semi-global asymptotic visual servoing result for unmanned aerial vehicles that tracked parallel coplanar linear visual features, while Zhang and Ostrowski [41] used a vision system to navigate a blimp.

In contrast to the previous image-based visual servo control approaches, novel homography-based visual servo control techniques have been recently developed in a series of papers by Malis and Chaumette (e.g., [26]–[28]). The homography-based approach exploits a combination of reconstructed Euclidean information and image-space information in the control design. The Euclidean information is reconstructed by decoupling the interaction between translation and rotation components of a homography matrix. As stated in [28], some advantages of this methodology over the aforementioned approaches are that an accurate Euclidean model of the environment (or target image) is not required and potential singularities in the image-Jacobian are eliminated (i.e., the image-Jacobian for homography-based visual servo controllers is typically triangular). Motivated by the advantages of the homography-based strategy, several researchers have recently developed various regulation controllers for robot manipulators (see [3], [5], [9], [13], and [15]). In [14], a homography-based visual servo control strategy was recently developed to asymptotically regulate the position/orientation of a WMR to a constant Euclidean position defined by a reference image, despite unknown depth information.

In this paper, a homography-based visual servo control strategy is used to force the Euclidean position/orientation of a camera mounted on an WMR (i.e., the camera-in-hand problem) to track a desired time-varying trajectory defined by a prerecorded sequence of images. Related research that focuses on vision-based controllers that focus on tracking a prerecorded sequence of images or reference path is provided in [29], [31], and [39]. By comparing the feature points of an object from a reference image to feature points of an object in the current image and the prerecorded sequence of images, projective geo-

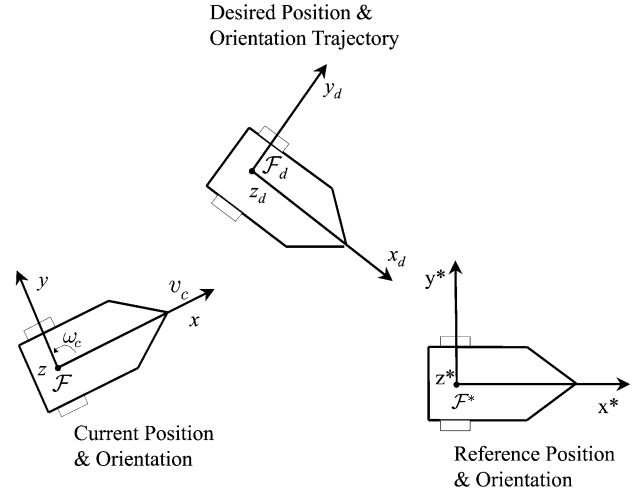


Fig. 1. Mobile robot coordinate systems.

metric relationships are exploited to enable the reconstruction of the Euclidean coordinates of the target points with respect to the WMR coordinate frame. The tracking control objective is naturally defined in terms of the Euclidean space, however, the translation error is unmeasurable, that is, the Euclidean reconstruction is scaled by an unknown distance from the camera/WMR to the target, and, while the scaled position is measurable through the homography, the unscaled position error is unmeasurable. To overcome this obstacle, a Lyapunov-based control strategy is employed that provides a framework for the construction of an adaptive update law to actively compensate for the unknown depth-related scaling constant. While similar techniques as in [14] are employed for the Euclidean reconstruction from the image data for the WMR system, a new development that is based on the preliminary research in [4] is presented in this paper to develop a tracking controller. In contrast to visual servo methods that linearize the system equations to facilitate EKF methods, the Lyapunov-based control design in this paper is based on the full nonlinear kinematic model of the vision system and the mobile robot system. Experimental results obtained from a modified Cybermotion K2A WMR testbed are presented to illustrate the performance of the controller.

II. PROBLEM FORMULATION

As illustrated in Fig. 1, the origin of the orthogonal coordinate system \mathcal{F} attached to the camera is coincident with the center of the WMR wheel axis (i.e., the camera is “in-hand”). As also illustrated in Fig. 1, the xy axis of \mathcal{F} defines the plane of motion where the x axis of \mathcal{F} is perpendicular to the wheel axis, and the y axis is parallel to the wheel axis. The z axis of \mathcal{F} is perpendicular to the plane of motion and is located at the center of the wheel axis. The linear velocity of the WMR along the x axis is denoted by $v_c(t) \in \mathbb{R}$, and the angular velocity $\omega_c(t) \in \mathbb{R}$ is about the z axis (see Fig. 1). The desired trajectory is defined by the prerecorded time-varying trajectory of \mathcal{F}_d that is assumed to be second-order differentiable. The desired trajectory is obtained from a prerecorded set of images of a stationary target viewed by the on-board camera as the WMR moves. For example, the desired WMR motion could be obtained as an operator drives the robot via a teach pendant, with the on-board camera capturing and storing the sequence of images of the stationary target. A fixed orthogonal coordinate system, denoted by \mathcal{F}^* , represents a fixed (i.e., a single snapshot) reference position and orientation of the camera relative to the stationary target. The introduction of \mathcal{F}^* is to enable the current and desired image trajectories to be compared to a

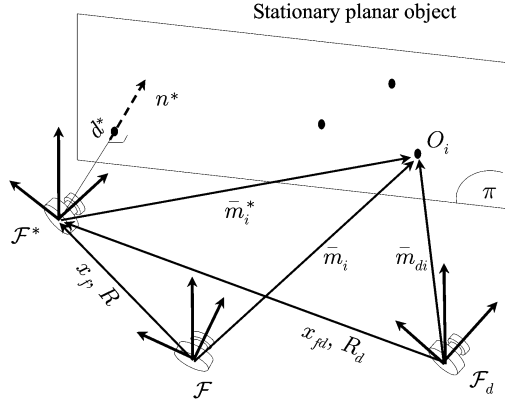


Fig. 2. Coordinate frame relationships.

constant reference image. The use of a constant reference image also facilitates the development of a constant parameter that can be related to the time-varying depth from the WMR to the target. Relating the time-varying depth information to a depth-related parameter facilitates adaptive control methods. Based on the definition of these coordinate frames, the goal of this paper is to develop a homography-based visual servo controller that will force \mathcal{F} to track the position and orientation trajectory provided by \mathcal{F}_d .

Remark 1: From a practical standpoint, numerous applications can be represented by the described problem formulation. For example, the WMR could be navigated via a teach pendant, while the camera records a desired set of images that represent the trajectory of the WMR relative to the target. Then, in subsequent tasks, the WMR will be able to track the same relative trajectory independent of the possibility that the target has moved between the time the image sequence was recorded and the autonomous task execution. A simple practical example is if the WMR is taught a path (via the set of images) to a docking station to recharge the batteries. The WMR will be able to track this path to achieve successful docking with the charging station independently of if the station has been moved from the original location (or, likewise, if the initial position and orientation of the WMR is different), provided obstacles have not been placed in the path of the WMR that would inhibit the WMR trajectory. See [31] for further discussion and motivation for the problem formulation.

A. Geometric Model

In this section, geometric relationships are developed between the coordinate systems \mathcal{F} , \mathcal{F}_d , and \mathcal{F}^* and a reference plane π that is defined by three target points $O_i \forall i = 1, 2, 3$ that are not collinear. The 3-D Euclidean coordinates of O_i expressed in terms of \mathcal{F} , \mathcal{F}_d , and \mathcal{F}^* as $\bar{m}_i(t)$, $\bar{m}_{di}(t)$, $\bar{m}_i^* \in \mathbb{R}^3$, respectively, are defined as follows (see Fig. 2):

$$\begin{aligned} \bar{m}_i(t) &\triangleq [x_i(t) \ y_i(t) \ z_i(t)]^T \\ \bar{m}_{di}(t) &\triangleq [x_{di}(t) \ y_{di}(t) \ z_{di}(t)]^T \\ \bar{m}_i^* &\triangleq [x_i^* \ y_i^* \ z_i^*]^T \end{aligned} \quad (1)$$

under the standard assumption that the distances from the origin of the respective coordinate frames to the targets along the focal axis remains positive (i.e., $x_i(t)$, $x_{di}(t)$, $x_i^* \geq \varepsilon > 0$ where ε is an arbitrarily small positive constant). The rotation from \mathcal{F}^* to \mathcal{F} is denoted by $R(t) \in SO(3)$, and the translation from \mathcal{F} to \mathcal{F}^* is denoted by $x_f(t) \in \mathbb{R}^3$ where $x_f(t)$ is expressed in \mathcal{F} . Similarly, $R_d(t) \in SO(3)$ denotes the

desired time-varying rotation from \mathcal{F}^* to \mathcal{F}_d , and $x_{fd}(t) \in \mathbb{R}^3$ denotes the desired translation from \mathcal{F}_d to \mathcal{F}^* , where $x_{fd}(t)$ is expressed in \mathcal{F}_d . Since the motion of the WMR is constrained to the xy plane, $x_f(t)$ and $x_{fd}(t)$ are defined as follows:

$$\begin{aligned} x_f(t) &\triangleq [x_{f1} \ x_{f2} \ 0]^T \\ x_{fd}(t) &\triangleq [x_{fd1} \ x_{fd2} \ 0]^T. \end{aligned} \quad (2)$$

From the geometry between the coordinate frames depicted in Fig. 2, \bar{m}_i^* can be related to $\bar{m}_i(t)$ and $\bar{m}_{di}(t)$ as follows:

$$\bar{m}_i = x_f + R\bar{m}_i^* \quad \bar{m}_{di} = x_{fd} + R_d\bar{m}_i^*. \quad (3)$$

In (3), $R(t)$ and $R_d(t)$ are defined as follows:

$$\begin{aligned} R &\triangleq \begin{bmatrix} \cos \theta & -\sin \theta & 0 \\ \sin \theta & \cos \theta & 0 \\ 0 & 0 & 1 \end{bmatrix} \\ R_d &\triangleq \begin{bmatrix} \cos \theta_d & -\sin \theta_d & 0 \\ \sin \theta_d & \cos \theta_d & 0 \\ 0 & 0 & 1 \end{bmatrix} \end{aligned} \quad (4)$$

where $\theta(t) \in \mathbb{R}$ denotes the right-handed rotation angle about $z_i(t)$ that aligns the rotation of \mathcal{F} with \mathcal{F}^* , and $\theta_d(t) \in \mathbb{R}$ denotes the right-handed rotation angle about $z_{di}(t)$ that aligns the rotation of \mathcal{F}_d with \mathcal{F}^* . From Fig. 1 and (4), it is clear that

$$\dot{\theta} = -\omega_c \quad \dot{\theta}_d = -\omega_{cd} \quad (5)$$

where $\omega_{cd}(t) \in \mathbb{R}$ denotes the desired angular velocity of the WMR expressed in \mathcal{F}_d . The rotation angles are assumed to be confined to the following regions:

$$-\pi < \theta(t) < \pi \quad -\pi < \theta_d(t) < \pi. \quad (6)$$

From the geometry given in Fig. 2, the distance $d^* \in \mathbb{R}$ from \mathcal{F}^* to π along the unit normal of π is given by

$$d^* = n^{*T} \bar{m}_i^* \quad (7)$$

where $n^* = [n_x^* \ n_y^* \ n_z^*]^T \in \mathbb{R}^3$ denotes the constant unit normal to π . Based on the definition of d^* in (7) and the fact that n^* and \bar{m}_i^* do not change, it is clear that d^* is a constant. From (7), the relationships in (3) can be expressed as follows:

$$\begin{aligned} \bar{m}_i &= \left(R + \frac{x_f n^{*T}}{d^*} \right) \bar{m}_i^* \\ \bar{m}_{di} &= \left(R_d + \frac{x_{fd} n^{*T}}{d^*} \right) \bar{m}_i^*. \end{aligned} \quad (8)$$

B. Euclidean Reconstruction

The relationship given in (3) provides a means to quantify the translational and rotational error between \mathcal{F} and \mathcal{F}^* and between \mathcal{F}_d and \mathcal{F}^* . Since the position of \mathcal{F} , \mathcal{F}_d , and \mathcal{F}^* cannot be directly measured, this section illustrates how the normalized Euclidean coordinates of the target points can be reconstructed by relating multiple images. Specifically, comparisons are made between an image acquired from the camera attached to \mathcal{F} , the reference image, and the prerecorded sequence of images that define the trajectory of \mathcal{F}_d . To facilitate the subsequent development, the normalized Euclidean coordinates of O_i

expressed in terms of \mathcal{F} , \mathcal{F}_d , and \mathcal{F}^* are denoted by $m_i(t)$, $m_{di}(t)$, $m_i^* \in \mathbb{R}^3$, respectively, are explicitly defined as follows:

$$\begin{aligned} m_i &\triangleq [1 \quad m_{iy} \quad m_{iz}]^T = \frac{\bar{m}_i}{x_i} \\ m_{di} &\triangleq [1 \quad m_{diy} \quad m_{diz}]^T = \frac{\bar{m}_{di}}{x_{di}} \\ m_i^* &\triangleq [1 \quad m_{iy}^* \quad m_{iz}^*]^T = \frac{\bar{m}_i^*}{x_i^*} \end{aligned} \quad (9)$$

where $\bar{m}_i(t)$, $\bar{m}_{di}(t)$, and \bar{m}_i^* were introduced in (1). In addition to having a Euclidean coordinate, each target point O_i will also have a projected pixel coordinate denoted by $u_i(t)$, $v_i(t) \in \mathbb{R}$ for \mathcal{F} , u_i^* , $v_i^* \in \mathbb{R}$ for \mathcal{F}^* , and $u_{di}(t)$, $v_{di}(t) \in \mathbb{R}$ for \mathcal{F}_d , that are defined as elements of $p_i(t) \in \mathbb{R}^3$ (i.e., the actual time-varying image points), $p_{di}(t) \in \mathbb{R}^3$ (i.e., the desired image point trajectory), and $p_i^* \in \mathbb{R}^3$ (i.e., the constant reference image points), respectively,

$$\begin{aligned} p_i &\triangleq [1 \quad v_i \quad u_i]^T \quad p_{di} \triangleq [1 \quad v_{di} \quad u_{di}]^T \\ p_i^* &\triangleq [1 \quad v_i^* \quad u_i^*]^T. \end{aligned} \quad (10)$$

The normalized Euclidean coordinates of the target points are related to the image data through the following pinhole lens models:

$$p_i = Am_i \quad p_{di} = Am_{di} \quad p_i^* = Am_i^* \quad (11)$$

where $A \in \mathbb{R}^{3 \times 3}$ is a known, constant, and invertible intrinsic camera calibration matrix.

Given that $m_i(t)$, $m_{di}(t)$, and m_i^* can be obtained from (11), the rotation and translation between the coordinate systems can now be related in terms of the normalized Euclidean coordinates as follows:

$$m_i = \underbrace{\frac{x_i^*}{x_i}}_{\alpha_i} \underbrace{(R + x_h n^{*T})}_H m_i^* \quad (12)$$

$$m_{di} = \underbrace{\frac{x_{di}^*}{x_{di}}}_{\alpha_{di}} \underbrace{(R_d + x_{hd} n^{*T})}_{H_d} m_i^* \quad (13)$$

where $\alpha_i(t)$, $\alpha_{di}(t) \in \mathbb{R}$ denote the depth ratios, $H(t)$, $H_d(t) \in \mathbb{R}^{3 \times 3}$ denote Euclidean homographies, and $x_h(t)$, $x_{hd}(t) \in \mathbb{R}^3$ denote scaled translation vectors that are defined as follows:

$$\begin{aligned} x_h &\triangleq [x_{h1} \quad x_{h2} \quad 0]^T = \frac{x_f}{d^*} \\ x_{hd} &\triangleq [x_{hd1} \quad x_{hd2} \quad 0]^T = \frac{x_{fd}}{d^*}. \end{aligned} \quad (14)$$

By using (4) and (14), the Euclidean homography in (12) can be rewritten as follows:

$$\begin{aligned} H &= [H_{jk}] \\ &= \begin{bmatrix} \cos \theta + x_{h1} n_x^* & -\sin \theta + x_{h1} n_y^* & x_{h1} n_z^* \\ \sin \theta + x_{h2} n_x^* & \cos \theta + x_{h2} n_y^* & x_{h2} n_z^* \\ 0 & 0 & 1 \end{bmatrix}. \end{aligned} \quad (15)$$

By examining the terms in (15), it is clear that $H(t)$ contains signals that are not directly measurable (e.g., $\theta(t)$, $x_h(t)$, and n^*). By expanding $H_{jk}(t) \forall j = 1, 2, k = 1, 2, 3$, the following expressions can be obtained from (9), (12), and (15):

$$1 = \alpha_i (H_{11} + H_{12} m_{iy}^* + H_{13} m_{iz}^*) \quad (16)$$

$$m_{iy} = \alpha_i (H_{21} + H_{22} m_{iy}^* + H_{23} m_{iz}^*) \quad (17)$$

$$m_{iz} = \alpha_i m_{iz}^*. \quad (18)$$

From (16)–(18), it is clear that three independent equations with nine unknowns (i.e., $H_{jk}(t) \forall j = 1, 2, k = 1, 2, 3$ and $\alpha_i(t) \forall i = 1, 2, 3$) can be generated for each target point. Hence, by determining the normalized Euclidean coordinate of three target points in \mathcal{F} and \mathcal{F}^* from the image data and (11), the unknown elements of $H(t)$ and the unknown ratio $\alpha_i(t)$ can be determined. Likewise, for the same three target points in \mathcal{F}_d and \mathcal{F}^* , the unknown elements of $H_d(t)$ and the unknown ratio $\alpha_{di}(t)$ can be determined. Once the elements of $H(t)$ and $H_d(t)$ are determined, various techniques (e.g., see [16] and [40]) can be used to decompose the Euclidean homographies to obtain the rotation and translation components. There are, in general, four solutions generated by the decomposition of $H(t)$ (and, likewise, for $H_d(t)$) depending on the multiplicity of the singular values. As stated in [16], some additional information (e.g., provided by the physical nature of the problem) must be used to determine the unique solution. For example, physical insight can be used to determine the unique solution among the four possible solutions for n^* (see Section V-B for details regarding one method to resolve the decomposition ambiguity). Hence, $R(t)$, $R_d(t)$, $x_h(t)$, and $x_{hd}(t)$ can all be computed and used for the subsequent control synthesis. Since $R(t)$ and $R_d(t)$ are known matrices, then (4) can be used to determine $\theta(t)$ and $\theta_d(t)$.

Remark 2: Motivation for using a homography-based approach is the desire to craft the error systems in a manner to facilitate the development of an adaptive update law to compensate for the unmeasurable depth parameter d^* , rather than infer depth from an object model. With the proposed approach, the mismatch between the estimated and actual depth information can be explicitly included in the stability analysis. Moreover, the resulting error systems do not depend on an image-Jacobian that could introduce singularities in the controller, which is an endemic problem with pure image-based visual servo control strategies.

Remark 3: To develop a tracking controller, it is typical that the desired trajectory is used as a feedforward component in the control design. Hence, for a kinematic controller, the desired trajectory is required to be at least first-order differentiable and at least second-order differentiable for a dynamic level controller. From the Euclidean homography introduced in (13), $m_d(t)$ can be expressed in terms of the *a priori* known functions $\alpha_{di}(t)$, $H_d(t)$, $R_d(t)$, and $x_{hd}(t)$. Since these signals can be obtained from the prerecorded sequence of images, sufficiently smooth functions can be generated for these signals by fitting a sufficiently smooth spline function to the signals. Hence, in practice, the *a priori* developed smooth functions $\alpha_{di}(t)$, $R_d(t)$, and $x_{hd}(t)$ can be constructed as bounded functions with sufficiently bounded time derivatives. Given $\theta_d(t)$ and the time derivative of $R_d(t)$, $\dot{\theta}_d(t)$ can be determined. In the subsequent tracking control development, $\dot{x}_{hd1}(t)$ and $\dot{\theta}_d(t)$ will be used in feedforward control terms.

III. CONTROL DEVELOPMENT

The control objective is to ensure that the coordinate frame \mathcal{F} tracks the time-varying trajectory of \mathcal{F}_d (i.e., $\bar{m}_i(t)$ tracks $\bar{m}_{di}(t)$). This objective is naturally defined in terms of the Euclidean position/orientation of the WMR. Specifically, based on the previous development, the translation and rotation tracking error, denoted by $e(t) \triangleq [e_1 \ e_2 \ e_3]^T \in \mathbb{R}^3$, is defined as follows:

$$\begin{aligned} e_1 &\triangleq x_{h1} - x_{hd1} \\ e_2 &\triangleq x_{h2} - x_{hd2} \\ e_3 &\triangleq \theta - \theta_d \end{aligned} \quad (19)$$

where $x_{h1}(t)$, $x_{h2}(t)$, $x_{hd1}(t)$, and $x_{hd2}(t)$ are introduced in (14), and $\theta(t)$ and $\theta_d(t)$ are introduced in (4). Based on the definition in (19), it

can be shown that the control objective is achieved if the tracking error $e(t) \rightarrow 0$. Specifically, it is clear from (14) that, if $e_1(t) \rightarrow 0$ and $e_2(t) \rightarrow 0$, then $x_f(t) \rightarrow x_{fd}(t)$. If $e_3 \rightarrow 0$, then it is clear from (4) and (19) that $R(t) \rightarrow R_d(t)$. If $x_f(t) \rightarrow x_{fd}(t)$ and $R(t) \rightarrow R_d(t)$, then (3) can be used to prove that $\bar{m}_i(t) \rightarrow \bar{m}_{di}(t)$.

A. Open-Loop Error System

As a means to develop the open-loop tracking error system, the time derivative of the Euclidean position $x_f(t)$ is determined as follows [28]:

$$\dot{x}_f = -v + [x_f]_{\times} \omega \quad (20)$$

where $v(t), \omega(t) \in \mathbb{R}^3$ denote the respective linear and angular velocity of the WMR expressed in \mathcal{F} as

$$v \triangleq [v_c \ 0 \ 0]^T \quad \omega \triangleq [0 \ 0 \ \omega_c]^T \quad (21)$$

and $[x_f]_{\times}$ denotes the 3×3 skew-symmetric form of $x_f(t)$. After substituting (14) into (20), the time derivative of the translation vector $x_h(t)$ can be written in terms of the linear and angular velocity of the WMR as follows:

$$\dot{x}_h = -\frac{v}{d^*} + [x_h]_{\times} \omega. \quad (22)$$

After incorporating (21) into (22), the following expression can be obtained:

$$\begin{aligned} \dot{x}_{h1} &= -\frac{v_c}{d^*} + x_{h2}\omega_c \\ \dot{x}_{h2} &= -x_{h1}\omega_c \end{aligned} \quad (23)$$

where (14) was utilized. Given that the desired trajectory is generated from a prerecorded set of images taken by the on-board camera as the WMR was moving, a similar expression as (20) can be developed as follows:

$$\dot{x}_{fd} = -[v_{cd} \ 0 \ 0]^T + [x_{fd}]_{\times} [0 \ 0 \ \omega_{cd}]^T \quad (24)$$

where $v_{cd}(t) \in \mathbb{R}$ denotes the desired linear¹ velocity of the WMR expressed in \mathcal{F}_d . After substituting (14) into (24), the time derivative of the translation vector $x_{hd}(t)$ can be written as follows:

$$\begin{aligned} \dot{x}_{hd1} &= -\frac{v_{cd}}{d^*} + x_{hd2}\omega_{cd} \\ \dot{x}_{hd2} &= -x_{hd1}\omega_{cd}. \end{aligned} \quad (25)$$

After taking the time derivative of (19) and utilizing (5) and (23), the following open-loop error system can be obtained:

$$\begin{aligned} d^* \dot{e}_1 &= -v_c + d^*(x_{h2}\omega_c - \dot{x}_{hd1}) \\ \dot{e}_2 &= -(x_{h1}\omega_c + x_{hd1}\dot{\theta}_d) \\ \dot{e}_3 &= -(\omega_c + \dot{\theta}_d) \end{aligned} \quad (26)$$

where the definition of $e_2(t)$ given in (19), and the second equation of (25) was utilized. To facilitate the subsequent development, the auxiliary variable $\bar{e}_2(t) \in \mathbb{R}$ is defined as

$$\bar{e}_2 \triangleq e_2 - x_{hd1}e_3. \quad (27)$$

¹Note that $v_{cd}(t)$ is not measurable.

After taking the time derivative of (27) and utilizing (26), the following expression is obtained:

$$\dot{\bar{e}}_2 = -(e_1\omega_c + \dot{x}_{hd1}e_3). \quad (28)$$

Based on (27), it is clear that, if $\bar{e}_2(t)$ and $e_3(t) \rightarrow 0$, then $e_2(t) \rightarrow 0$. Based on this observation and the open-loop dynamics given in (28), the following control development is based on the desire to prove that $e_1(t), \bar{e}_2(t), e_3(t)$ are asymptotically driven to zero.

B. Closed-Loop Error System

Based on the open-loop error systems in (26) and (28), the linear and angular velocity kinematic control inputs for the WMR are designed as follows:

$$v_c \triangleq k_v e_1 - \bar{e}_2 \omega_c + \hat{d}^*(x_{h2}\omega_c - \dot{x}_{hd1}) \quad (29)$$

$$\omega_c \triangleq k_\omega e_3 - \dot{\theta}_d - \dot{x}_{hd1} \bar{e}_2 \quad (30)$$

where $k_v, k_\omega \in \mathbb{R}$ denote positive, constant control gains. In (29), the parameter update law $\hat{d}^*(t) \in \mathbb{R}$ is generated by the following differential equation:

$$\dot{\hat{d}}^* = \gamma_1 e_1 (x_{h2}\omega_c - \dot{x}_{hd1}) \quad (31)$$

where $\gamma_1 \in \mathbb{R}$ is a positive, constant adaptation gain. After substituting the kinematic control signals designed in (29) and (30) into (26), the following closed-loop error systems are obtained:

$$\begin{aligned} d^* \dot{e}_1 &= -k_v e_1 + \bar{e}_2 \omega_c + \tilde{d}^*(x_{h2}\omega_c - \dot{x}_{hd1}) \\ \dot{\bar{e}}_2 &= -(e_1 \omega_c + \dot{x}_{hd1} e_3) \\ \dot{e}_3 &= -k_\omega e_3 + \dot{x}_{hd1} \bar{e}_2 \end{aligned} \quad (32)$$

where (28) was utilized, and the depth-related parameter estimation error $\tilde{d}^*(t) \in \mathbb{R}$ is defined as follows:

$$\tilde{d}^* \triangleq d^* - \hat{d}^*. \quad (33)$$

IV. STABILITY ANALYSIS

Theorem 1: The adaptive update law defined in (31) along with the control input designed in (29) and (30) ensure that the WMR tracking error $e(t)$ is asymptotically driven to zero in the sense that

$$\lim_{t \rightarrow \infty} e(t) = 0 \quad (34)$$

provided that the time derivative of the desired trajectory satisfies the following condition:

$$\lim_{t \rightarrow \infty} \dot{x}_{hd1} \neq 0. \quad (35)$$

Proof: To prove Theorem 1, the nonnegative function $V(t) \in \mathbb{R}$ is defined as follows:

$$V \triangleq \frac{1}{2} d^* e_1^2 + \frac{1}{2} \bar{e}_2^2 + \frac{1}{2} e_3^2 + \frac{1}{2\gamma_1} \tilde{d}^{*2}. \quad (36)$$

The following simplified expression can be obtained by taking the time derivative of (36), substituting the closed-loop dynamics in (32) into the resulting expression, and then cancelling common terms

$$\dot{V} = -k_v e_1^2 + e_1 \dot{d}^* (x_{hd2} \omega_c - \dot{x}_{hd1}) - k_\omega e_3^2 - \frac{1}{\gamma_1} \dot{d}^* \dot{d}^*. \quad (37)$$

After substituting (31) into (37), the following expression can be obtained:

$$\dot{V} = -k_v e_1^2 - k_\omega e_3^2. \quad (38)$$

From (36) and (38), it is clear that $e_1(t), \bar{e}_2(t), e_3(t), \dot{d}^*(t) \in \mathcal{L}_\infty$ and that $e_1(t), e_3(t) \in \mathcal{L}_2$. Since $\dot{d}^*(t) \in \mathcal{L}_\infty$ and d^* is a constant, the expression in (33) can be used to determine that $\dot{d}^*(t) \in \mathcal{L}_\infty$. From the assumption that $x_{hd1}(t), \dot{x}_{hd1}(t), x_{hd2}(t), \theta_d(t)$, and $\dot{\theta}_d(t)$ are constructed as bounded functions, and the fact that $\bar{e}_2(t), e_3(t) \in \mathcal{L}_\infty$, the expressions in (19), (27), and (30) can be used to prove that $e_2(t), x_{h1}(t), x_{h2}(t), \theta(t), \omega_c(t) \in \mathcal{L}_\infty$. Based on the previous development, the expressions in (29), (31), and (32) can be used to conclude that $v_c(t), \dot{d}^*(t), \dot{e}_1(t), \dot{\bar{e}}_2(t), \dot{e}_3(t) \in \mathcal{L}_\infty$. Based on the fact that $e_1(t), e_3(t), \dot{e}_1(t), \dot{e}_3(t) \in \mathcal{L}_\infty$ and that $e_1(t), e_3(t) \in \mathcal{L}_2$, Barbalat's Lemma [32] can be employed to prove that

$$\lim_{t \rightarrow \infty} e_1(t), \quad e_3(t) = 0. \quad (39)$$

From (39) and the fact that the signal $(\dot{x}_{hd1}(t)\bar{e}_2(t))$ is uniformly continuous (i.e., $\dot{x}_{hd1}(t), \ddot{x}_{hd1}(t), \bar{e}_2(t), \dot{\bar{e}}_2(t) \in \mathcal{L}_\infty$), the Extended Barbalat's Lemma (see the Appendix) can be applied to the last equation in (32) to prove that

$$\lim_{t \rightarrow \infty} \dot{e}_3(t) = 0 \quad (40)$$

and that

$$\lim_{t \rightarrow \infty} \dot{x}_{hd1}(t)\bar{e}_2(t) = 0. \quad (41)$$

If the desired trajectory satisfies (35), then (41) can be used to prove that

$$\lim_{t \rightarrow \infty} \bar{e}_2(t) = 0. \quad (42)$$

Based on the definition of $\bar{e}_2(t)$ given in (27), the results in (39) and (42) can be used to conclude that

$$\lim_{t \rightarrow \infty} e_2(t) = 0 \quad (43)$$

provided that the condition in (35) is satisfied. \square

Remark 4: The condition given in (35) is in terms of the time derivative of the desired translation vector. Typically, for WMR tracking problems, this assumption is expressed in terms of the desired linear and angular velocity of the WMR. To this end, (25) can be substituted into (35) to obtain the following condition:

$$\lim_{t \rightarrow \infty} \frac{v_{cd}(t)}{d^*} \neq x_{hd2}(t)\omega_{cd}(t). \quad (44)$$



Fig. 3. WMR testbed.

The condition in (44) is comparable to typical WMR tracking results that restrict the desired linear and angular velocity. For an in-depth discussion of this type of restriction, including related previous results, see [12].

V. EXPERIMENTAL VERIFICATION

A. Experimental Configuration

To implement the adaptive tracking controller given by (29)–(31), an experimental testbed (see Fig. 3) was constructed. The WMR testbed consists of the following components: a modified K2A WMR (with an inclusive Pentium 133-MHz PC) manufactured by Cybermotion Inc., a Dalsa CAD-6 camera that captures 955 frames per second with 8-bit gray scale at a 260×260 resolution, a Road Runner Model 24 video capture board, and two Pentium-based PCs. In addition to the WMR modifications described in detail in [12], additional modifications particular to this experiment included mounting a camera and the associated image processing Pentium IV 800-MHz PC (operating under QNX, a real-time micro-kernel-based operating system) on the top of the WMR as depicted in Fig. 3. The internal WMR computer (also operating under QNX) hosts the control algorithm that was written in “C/C++” and implemented using Qmotor 3.0 [23]. In addition to the image-processing PC, a second PC (operating under the MS Windows 2000 operating system) was used to remotely log in to the internal WMR PC via the QNX Phindows application. The remote PC was used to access the graphical user interface of Qmotor for execution of the control program, gain adjustment, and data management, plotting, and storage. Three light-emitting diodes (LEDs) were rigidly attached to a rigid structure that was used as the target, where the intensity of the LEDs contrasted sharply with the background. Due to the intensity contrast, a simple thresholding algorithm was used to determine the coordinates of the centroid of the region of brightness values associated with each LED. The centroid was selected as the coordinates of the feature point.

The WMR is controlled by a torque input applied to the drive and steer motors. As subsequently described, to facilitate a torque controller, the actual linear and angular velocity of the WMR is required.

To acquire these signals, a backward difference algorithm was applied to the drive and steering motor encoders. Encoder data acquisition and the control implementation were performed at a frequency of 1.0 kHz using the Quanser MultiQ I/O board. For simplicity, the electrical and mechanical dynamics of the system were not incorporated in the control design (i.e., the emphasis of this experiment is to illustrate the visual servo controller). However, since the developed kinematic controller is differentiable, standard backstepping techniques could be used to incorporate the mechanical and electrical dynamics. See [10] and [12] for several examples that incorporate the mechanical dynamics. Permanent magnet dc motors provide steering and drive actuation through a 106:1 and a 96:1 gear coupling, respectively. The dynamics for the modified K2A WMR are given as follows:

$$\frac{1}{r_o} \begin{bmatrix} 1 & 0 \\ 0 & \frac{L_o}{2} \end{bmatrix} \begin{bmatrix} \tau_1 \\ \tau_2 \end{bmatrix} = \begin{bmatrix} m_o & 0 \\ 0 & I_o \end{bmatrix} \begin{bmatrix} \dot{v}_1 \\ \dot{v}_2 \end{bmatrix} \quad (45)$$

where $\tau_1(t), \tau_2(t) \in \mathbb{R}$ denote the drive and steering motor torques, respectively, $m_o = 165$ kg denotes the mass of the robot, $I_o = 4.643$ kg·m² denotes the inertia of the robot, $r_o = 0.010$ m denotes the radius of the wheels, and $L_o = 0.667$ m denotes the length of the axis between the wheels.

B. Experimental Results

To acquire the desired image trajectory, the WMR was driven by a joystick while the image-processing PC acquired the camera images at 955 frames/s, which is determined the pixel coordinates of the feature points, and saved the pixel data to a file. The last image was also saved as the reference image. The desired image file and the reference image were read into a stand-alone program that computed $x_{hd}(t)$ and $\theta_d(t)$ offline. To determine the unique solution for $x_{hd}(t)$ and $\theta_d(t)$ (and, likewise, for $x_h(t)$ and $\theta(t)$) from the set of possible solutions generated by the homography decomposition using the Faugeras decomposition algorithm, a best-guess estimate of the constant normal n^* was selected as $n^* = [1 \ 0 \ 0]^T$ (i.e., from the physical relationship between the camera and the plane defined by the object feature points, the focal axis of the camera mounted on the WMR was assumed to be roughly perpendicular to π). Of the possible solutions generated for n^* by the decomposition algorithm, the solution that yielded the minimum norm difference with the initial best guess was determined as the correct solution. The solution that most closely matched the best-guess estimate was then used to determine the correct solutions for $x_{hd}(t)$ and $\theta_d(t)$ (or $x_h(t)$ and $\theta(t)$). The robustness of the system is not affected by the *a priori* estimate of n^* since the estimate is only used to resolve the ambiguity in the solutions generated by the decomposition algorithm, and the n^* generated by the decomposition algorithm is used to further decompose the homography. A Butterworth filter was applied to $x_{hd}(t)$ and $\theta_d(t)$ to reduce noise effects. A filtered backward difference algorithm was used to compute $\dot{x}_{hd}(t)$ and $\dot{\theta}_d(t)$. Figs. 4 and 5 depict the desired translation and rotation signals, respectively.

The desired trajectory signals $x_{hd}(t)$, $\dot{x}_{hd}(t)$, $\theta_d(t)$, and $\dot{\theta}_d(t)$ were stored in a file that was opened by the control algorithm and loaded into memory when the control algorithm was loaded in Qmotor. Before the control program was executed, the image-processing PC was set to acquire the live camera images at 955 frames/s, determine the pixel coordinates of the feature points, and transmit the coordinates via a server program over a dedicated 100-Mb/s network connection to the internal WMR computer. A client program was executed on the internal WMR computer to receive the pixel coordinates from the server program and write the current pixel information into a shared memory location. When the control program was executed, the current image information was acquired from the shared memory loca-

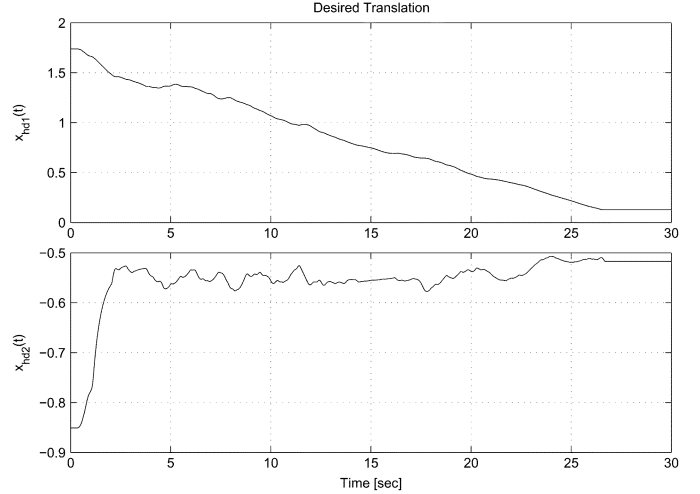


Fig. 4. Desired translation.

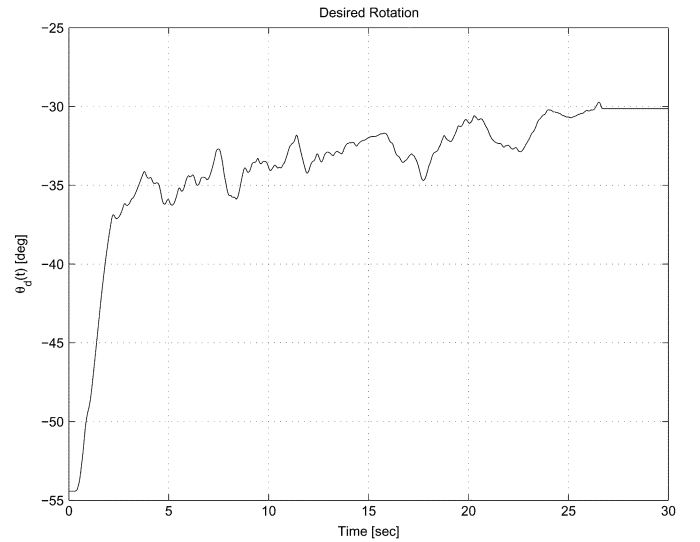


Fig. 5. Desired rotation.

tion (rather than directly from the network connection to maintain deterministic response and for program stability) and was compared to the reference image for online computation of the Euclidean homography. The homography was decomposed using the Faugeras decomposition algorithm [16] to determine $x_h(t)$ and $\theta(t)$. After determining $x_h(t)$ and $\theta(t)$, comparisons with $x_{hd}(t)$ and $\theta_d(t)$ were made at each time instant to compute the error signal $e_1(t)$, $e_2(t)$, and $e_3(t)$, which were subsequently used to compute $v_c(t)$, $\omega_c(t)$, and $\hat{d}^*(t)$ given in (29)–(31). To execute a torque level controller, a high-gain feedback loop was implemented as follows:

$$\tau = \bar{K}_h \eta \quad (46)$$

where $\bar{K}_h \in \mathbb{R}^{2 \times 2}$ is a diagonal high-gain feedback term and $\eta(t) \in \mathbb{R}^2$ is a velocity mismatch signal defined as

$$\eta = [v_c \ \omega_c]^T - [v_a \ \omega_a]^T \quad (47)$$

where $v_c(t)$ and $\omega_c(t)$ denote the linear and angular velocity inputs computed in (29) and (30) and $v_a(t)$ and $\omega_a(t)$ denote actual linear

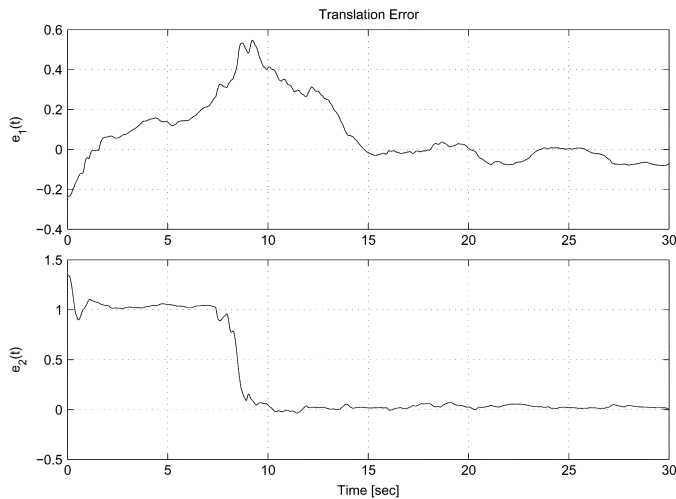


Fig. 6. Translation error.

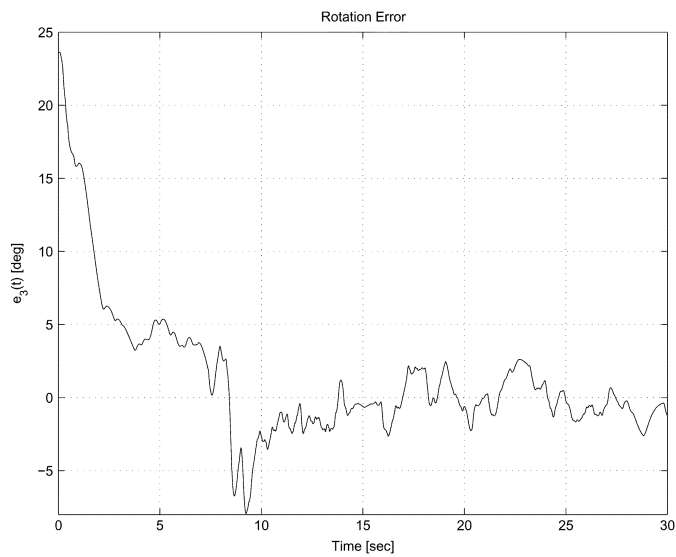


Fig. 7. Rotation error.

and angular velocity of the WMR computed from the time derivative of the wheel encoders.

The control gains were adjusted to reduce the position/orientation tracking error with the adaptation gains set to zero and the initial adaptive estimate set to zero. After some tuning, we noted that the position/orientation tracking error response could not be significantly improved by further adjustments of the feedback gains. We then adjusted the adaptation gains to allow the parameter estimation to reduce the position/orientation tracking error. After the tuning process was completed, the final adaptation and feedback gain values were recorded as follows:

$$\begin{aligned} k_v &= 4.15, & k_\omega &= 0.68, & \gamma &= 40.1, \\ K_h &= \text{diag}\{99.7, 23.27\}. \end{aligned} \quad (48)$$

The unitless position/orientation tracking errors $e_1(t)$ and $e_2(t)$ are depicted in Figs. 6 and 7, respectively. Fig. 8 illustrates that the adaptive estimate for the depth parameter d^* approaches a constant. Fig. 9 illustrates the linear and angular velocity of the WMR. The control torque inputs are presented in Fig. 10 and represent the torques applied after the gearing mechanism.

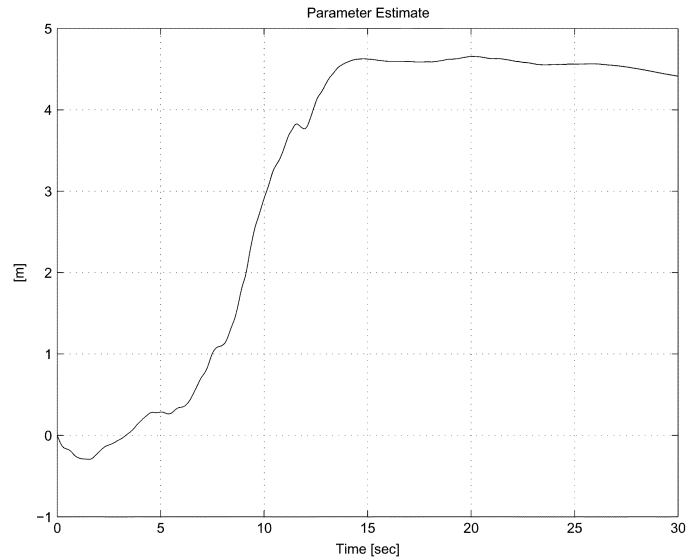


Fig. 8. Parameter estimate.

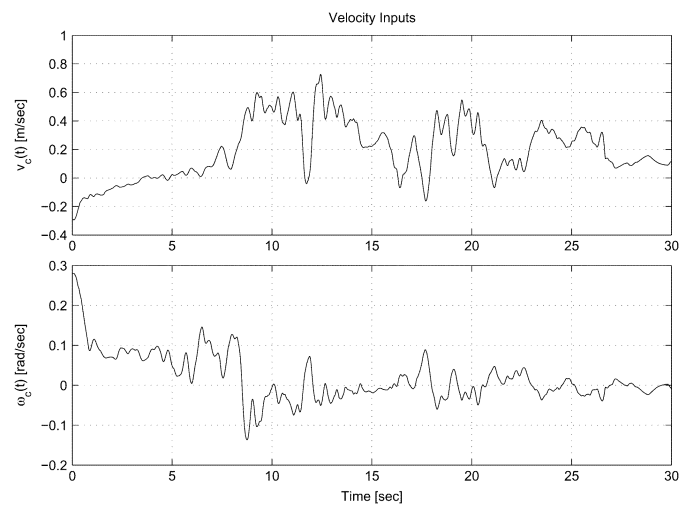


Fig. 9. Linear and angular velocity control inputs.

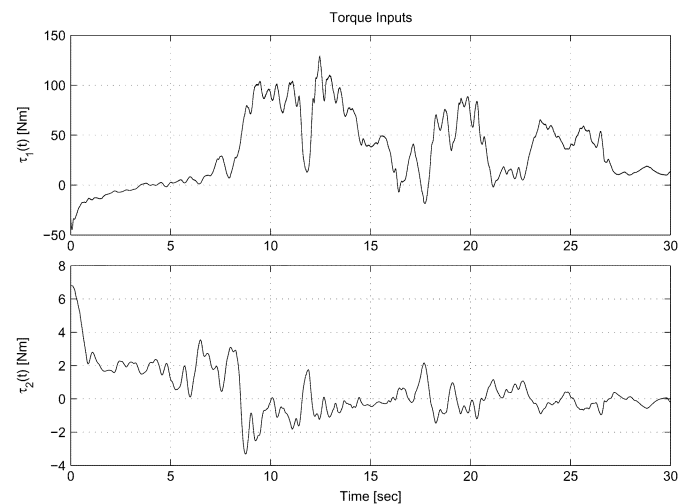


Fig. 10. Drive and steer motor torque inputs.

C. Results Discussion

From Figs. 6 and 7, it is clear that $e_2(t)$ is relatively unchanging in the first 8 s, whereas $e_1(t)$ and $e_3(t)$ are changing significantly. This phenomena is due to the nonholonomic nature of the vehicle. Specifically, since there is an initial position and orientation error, the controller moves the vehicle to minimize the error and align the WMR with the desired image trajectory. Since the WMR cannot move along both axes of the Cartesian plane simultaneously while also rotating (i.e., due to the nonholonomic motion constraints), the WMR initially moves to minimize $e_1(t)$ and $e_3(t)$. Likewise, when $e_2(t)$ undergoes change between 8 and 10 s, $e_1(t)$ remains relatively unchanging. While performing the experiment, slightly different responses were obtained each run due to variations in the initial position and orientation of the WMR and variations in the control parameters as the gains were adjusted. With a constant set of control gains, the transient response still exhibited some variations due to differences in the initial conditions, however, the steady-state response remained constant for each trial.

Note that $e_1(t)$ and $e_2(t)$ depicted in Fig. 6 are unitless. From (14) and (19), it is clear that $e_1(t)$ and $e_2(t)$ are unitless because the translation $x_f(t)$ has units of meters, and the depth-related constant d^* has units of meters, that is, $x_h(t)$ and $x_{h,d}(t)$ are unitless translation terms computed from the homography decomposition (note that no units are provided in Fig. 4). In practice, the WMR traversed an arc that approximately spanned a $6 \times 1 - \text{m}^2$ space, with an approximate speed of 0.22 m/s (i.e., approximately the same speed as the numerous WMR experiments presented in [12]).

Based on the outcome of this experiment, several issues for future research and technology integration are evident. For example, the problem formulation in this paper has a number of practical applications in environments where the reference object may not be stationary between each task execution (e.g., the example described in Remark 1). However, the result in this paper does not address cases where an obstacle enters the task space and inhibits the WMR from tracking the prerecorded trajectory. To address this issue, there is a clear need for continued research that targets incorporating image-space path planning with the control design as in [6], [7], [17], and [30]. Additionally, the result in this paper does not address a method to automatically reselect feature points. For example, methods to automatically determine new feature points if they become nearly aligned or if a feature point leaves the field of view (e.g., becomes occluded) could add robustness to the implemented control system. Of course, an *ad hoc* approach of simply continuously tracking multiple redundant feature points could be utilized, but this approach may excessively restrict the image processing bandwidth.

VI. CONCLUSION

In this paper, the position/orientation of a WMR is forced to track a desired time-varying trajectory defined by a prerecorded sequence of images. To achieve the result, multiple views of three target points were used to develop Euclidean homographies. By decomposing the Euclidean homographies into separate translation and rotation components, reconstructed Euclidean information was obtained for the control development. A Lyapunov-based stability argument was used to design an adaptive update law to compensate for the fact that the reconstructed translation signal was scaled by an unknown depth parameter. The impact that the development in this paper makes is that a new analytical approach has been developed using homography-based concepts to enable the position/orientation of a WMR subject to nonholonomic constraints to track a desired trajectory generated from a sequence of images, despite the lack of depth measurements. Experimental results are provided to illustrate the performance of the controller.

APPENDIX

The Extended Barbalat's Lemma was utilized in the stability analysis for Theorem 1. This lemma stated as follows, and a proof for the Lemma can be found in [12].

Lemma 1:

If a differentiable function $f(t) \in \mathbb{R}$ has a finite limit as $t \rightarrow \infty$ and its time derivative can be written as follows:

$$\dot{f}(t) = g_1(t) + g_2(t) \quad (49)$$

where $g_1(t)$ is a uniformly continuous function and

$$\lim_{t \rightarrow \infty} g_2(t) = 0 \quad (50)$$

then

$$\lim_{t \rightarrow \infty} \dot{f}(t) = 0 \quad \text{and} \quad \lim_{t \rightarrow \infty} g_1(t) = 0. \quad (51)$$

REFERENCES

- [1] S. Baker and S. Nayar, "A theory of catadioptric image formation," in *Proc. ICCV*, Bombay, India, Jan. 1998, pp. 35–42.
- [2] D. Burschka and G. Hager, "Vision-based control of mobile robots," in *Proc. IEEE Int. Conf. Robot. Autom.*, Seoul, Korea, May 2001, pp. 1707–1713.
- [3] J. Chen, A. Behal, D. Dawson, and Y. Fang, "2.5D visual servoing with a fixed camera," in *Proc. IEEE Amer. Control Conf.*, Denver, CO, June 2003, pp. 3442–3447.
- [4] J. Chen, W. E. Dixon, D. M. Dawson, and M. McIntire, "Homography-based visual servo tracking control of a wheeled mobile robot," in *Proc. IEEE/RSJ Int. Conf. Intell. Robots Syst.*, Las Vegas, NV, Oct. 2003, pp. 1814–1819.
- [5] P. I. Corke and S. A. Hutchinson, "A new hybrid image-based visual servo control scheme," in *Proc. IEEE Conf. Decision Control*, Las Vegas, NV, Dec. 2000, pp. 2521–2527.
- [6] N. J. Cowan, O. Shakernia, R. Vidal, and S. Sastry, "Vision-based follow-the-leader," in *Proc. Int. Conf. Intell. Robots Syst.*, Las Vegas, NV, Oct. 2003, pp. 1796–1801.
- [7] N. J. Cowan, J. D. Weingarten, and D. E. Koditschek, "Visual servoing via navigation function," *IEEE Trans. Robot. Autom.*, vol. 18, no. 4, pp. 521–53, Aug. 2002.
- [8] A. K. Das, R. Fierro, R. V. Kumar, B. Southall, J. R. Spletzer, and C. J. Taylor, "Realtime vision-based control of a nonholonomic mobile robot," in *Proc. IEEE Int. Conf. Robot. Autom.*, Seoul, Korea, May 2001, pp. 1714–1719.
- [9] K. Deguchi, "Optimal motion control for image-based visual servoing by decoupling translation and rotation," in *Proc. Int. Conf. Intell. Robots Syst.*, Victoria, BC, Canada, Oct. 1998, pp. 705–711.
- [10] W. E. Dixon, M. S. de Queiroz, D. M. Dawson, and T. J. Flynn, "Adaptive tracking and regulation control of a wheeled mobile robot with controller/update law modularity," *IEEE Trans. Control Syst. Technol.*, vol. 12, no. 1, pp. 138–147, Mar. 2004.
- [11] W. E. Dixon, D. M. Dawson, E. Zergeroglu, and A. Behal, "Adaptive tracking control of a wheeled mobile robot via an uncalibrated camera system," *IEEE Trans. Syst., Man, Cybern. B: Cybern.*, vol. 31, no. 3, pp. 341–352, Jun. 2001.
- [12] —, *Nonlinear Control of Wheeled Mobile Robots*. London, U.K.: Springer-Verlag, 2001.
- [13] Y. Fang, A. Behal, W. E. Dixon, and D. M. Dawson, "Adaptive 2.5D visual servoing of kinematically redundant robot manipulators," in *Proc. IEEE Conf. Decision Control*, Las Vegas, NV, Dec. 2002, pp. 2860–2865.
- [14] Y. Fang, D. M. Dawson, W. E. Dixon, and M. S. de Queiroz, "2.5D visual servoing of wheeled mobile robots," in *Proc. IEEE Conf. Decision Control*, Las Vegas, NV, Dec. 2002, pp. 2866–2871.

- [15] Y. Fang, W. E. Dixon, D. M. Dawson, and J. Chen, "Robust 2.5D visual servoing for robot manipulators," in *Proc. IEEE Amer. Control Conf.*, Denver, CO, Jun. 2003, pp. 3311–3316.
- [16] O. Faugeras, *Three-Dimensional Computer Vision*. Cambridge, MA: MIT Press, 2001.
- [17] N. R. Gans and S. A. Hutchinson, "An asymptotically stable switched system visual controller for eye in hand robots," in *Proc. IEEE/RJS Int. Conf. Intell. Robots Syst.*, Las Vegas, NV, Oct. 2003, pp. 735–742.
- [18] G. D. Hagar, D. J. Kriegman, A. S. Georgiades, and O. Ben-Shahar, "Toward domain-independent navigation: dynamic vision and control," in *Proc. IEEE Conf. Decision Control*, Tampa, FL, Dec. 1998, pp. 3257–3262.
- [19] M. Hebert and T. Kanade, "3-D vision for outdoor navigation by an autonomous vehicle," in *Proc. Image Understanding Workshop*, San Mateo, CA, Apr. 1988, pp. 593–601.
- [20] Y. Kanayama, Y. Kimura, F. Miyazaki, and T. Noguchi, "A stable tracking control method for an autonomous mobile robot," in *Proc. IEEE Int. Conf. Robot. Autom.*, Cincinnati, OH, May 1990, pp. 253–258.
- [21] B. H. Kim *et al.*, "Localization of a mobile robot using images of a moving target," in *Proc. IEEE Int. Conf. Robot. Autom.*, Seoul, Korea, May 2001, pp. 253–258.
- [22] D. J. Kriegman, E. Triendl, and T. O. Binford, "Stereo vision navigation in buildings for mobile robots," *IEEE Trans. Robot. Autom.*, vol. 5, no. 6, pp. 792–803, Dec. 1989.
- [23] M. S. Loffler, N. P. Costescu, and D. M. Dawson, "QMOTOR 3.0 and the QMotor robotic toolkit: a PC-based control platform," *IEEE Control Syst. Mag.*, vol. 22, no. 3, pp. 12–26, 2002.
- [24] Y. Ma, J. Kosecka, and S. Sastry, "Vision guided navigation for non-holonomic mobile robot," *IEEE Trans. Robot. Autom.*, vol. 15, no. 3, pp. 521–536, Jun. 1999.
- [25] R. Mahony and T. Hamel, "Visual servoing using linear features for under-actuated rigid body dynamics," in *Proc. IEEE/RJS Int. Conf. Intell. Robots Syst.*, Oct./Nov. 2001, pp. 1153–1158.
- [26] E. Malis and F. Chaumette, "Theoretical improvements in the stability analysis of a new class of model-free visual servoing methods," *IEEE Trans. Robot. Autom.*, vol. 18, no. 2, pp. 176–186, Apr. 2002.
- [27] ———, "2 1/2 D visual servoing with respect to unknown objects through a new estimation scheme of camera displacement," *Int. J. Comput. Vis.*, vol. 37, no. 1, pp. 79–97, 2000.
- [28] E. Malis, F. Chaumette, and S. Bodet, "2 1/2 D visual servoing," *IEEE Trans. Robot. Autom.*, vol. 15, no. 2, pp. 238–250, Apr. 1999.
- [29] Y. Matsutomo, M. Inaba, and H. Inoue, "Visual navigation using view-sequence route representation," in *Proc. IEEE Int. Conf. Robot. Autom.*, Minneapolis, MN, Apr. 1996, pp. 83–88.
- [30] Y. Mezouar and F. Chaumette, "Path planning for robust image-based control," *IEEE Trans. Robot. Autom.*, vol. 18, no. 4, pp. 534–549, Aug. 2002.
- [31] S. B. Skaar and J. D. Yoder, "Extending teach-repeat to nonholonomic robots," *Structronic Syst.: Smart Structures, Devices Syst. II*, ser. Stability, Vibration and Control of Systems, vol. 4, pp. 316–342, 1998.
- [32] J. J. E. Slotine and W. Li, *Applied Nonlinear Control*. Englewood Cliffs, NJ: Prentice-Hall, 1991.
- [33] K.-T. Song and J.-H. Huang, "Fast optical flow estimation and its application to real-time obstacle avoidance," in *Proc. IEEE Int. Conf. Robot. Autom.*, Seoul, Korea, May 2001, pp. 2891–2896.
- [34] C. E. Thorpe, M. Hebert, T. Kanade, and S. Shafer, "Vision and navigation for the Carnegie-Mellon Navlab," *IEEE Trans. Pattern Anal. Mach. Intell.*, vol. 10, no. 3, pp. 362–373, Mar. 1988.
- [35] D. Tsakiris, P. Rives, and C. Samson, "Extending visual servoing techniques to nonholonomic mobile robots," in *The Confluence of Vision and Control, Lecture Notes in Control and Information Systems*, D. Kriegman, Ed. Berlin, Germany: Springer-Verlag, 1998, pp. 107–117.
- [36] M. A. Turk, D. G. Morgenthaler, K. D. Gremban, and M. Marra, "VITS—a vision system for autonomous land vehicle navigation," *IEEE Trans. Pattern Anal. Mach. Intell.*, vol. 10, no. 3, pp. 342–361, Mar. 1988.
- [37] H. Y. Wang, S. Itani, T. Fukao, and N. Adachi, "Image-based visual adaptive tracking control of nonholonomic mobile robots," in *Proc. IEEE/RJS Int. Conf. Intell. Robots Syst.*, Oct./Nov. 2001, pp. 1–6.
- [38] A. M. Waxman, "A visual navigation system for autonomous land vehicles," *IEEE J. Robot. Autom.*, vol. RA-3, no. 2, pp. 124–141, Apr. 1987.
- [39] J. D. Yoder, E. T. Baumgartner, and S. B. Skaar, "Initial results in the development of a guidance system for a powered wheelchair," *IEEE Trans. Rehabil. Eng.*, vol. 4, no. 3, pp. 143–151, 1996.
- [40] Z. Zhang and A. R. Hanson, "Scaled euclidean 3D reconstruction based on externally uncalibrated cameras," in *Proc. IEEE Symp. Comput. Vis.*, 1995, pp. 37–42.
- [41] H. Zhang and J. P. Ostrowski, "Visual servoing with dynamics: control of an unmanned blimp," in *Proc. IEEE Int. Conf. Robot. Autom.*, May 1999, pp. 618–623.

Statistically Robust 2-D Visual Servoing

Andrew I. Comport, Éric Marchand, and François Chaumette

Abstract—A fundamental step toward broadening the use of real-world image-based visual servoing is to deal with the important issue of reliability and robustness. In order to address this issue, a closed-loop control law is proposed that simultaneously accomplishes a visual servoing task and is robust to a general class of image processing errors. This is achieved with the application of widely accepted statistical techniques such as robust M-estimation and LMedS. Experimental results are presented which demonstrate visual servoing tasks that resist severe outlier contamination.

Index Terms—Least median squares (LMedS), M-estimators, robust control law, visual servoing.

I. INTRODUCTION

Visual servoing is known to be a very efficient method for positioning and target tracking tasks [1]. However, its efficiency relies on correspondences between the position of tracked visual features in the current image and their position in the desired image, which define a set of errors to be minimized. If these correspondences contain errors, then visual servoing usually fails or converges upon a wrong position.

Overcoming these errors is often achieved by improving the quality of tracking algorithms [2]–[4] and feature selection methods [5]. This class of methods uses information measurements which are not directly related to the set of errors but based on external cues such as color and global motion estimation. These approaches provide a robust input estimate to the control loop, and, as such treats outlier rejection in the image processing step, prior to the control step [see Fig. 1(a)]. Considering redundant features [6] is also a simple way to improve positioning accuracy and reduce the sensitivity to noise. However, it cannot allow to suppress completely the final positioning error in the presence of erroneous data.

Alternatively, the method proposed in this paper is based on a well-founded and efficient formalism which directly uses the feature error vector to compute a statistical measure of confidence *at the control law level* [see Fig. 1(b)]. In related literature, many different approaches exist to treat external sources of error. Amongst the robust outlier rejection algorithms [7], methods in computer vision have included the

Manuscript received April 25, 2005; revised September 28, 2005. This paper was recommended for publication by Associate Editor B. Nelson and Editor S. Hutchinson upon evaluation of the reviewers' comments. This paper was presented in part at the IEEE International Conference on Intelligent Robots and Systems, Las Vegas, NV, October 2003, and in part at the IEEE International Conference on Robotics and Automation, New Orleans, LA, April 2004.

The authors are with IRISA-INRIA Rennes, 35042 Rennes Cedex, France (e-mail: Eric.Marchand@irisa.fr; chaumett@irisa.fr).

Digital Object Identifier 10.1109/TRO.2006.870666